International Journal of Fluid Machinery and Systems
Vol. 9, No. 2, April-June 2016

DOI: http://dx.doi.org/10.5293/IJFMS.2016.9.2.119
ISSN (Online): 1882-9554

Original Paper

Numerical Analysis of Unsteady Cavitating Flow around Balancing Drum of Multistage Pump

Milan Sedlář[1], Tomáš Krátký[1] and Patrik Zima[2]

[1]Centre of Hydraulic Research, spol. s r. o.
Jana Sigmunda 190, Lutín, 783 49, Czech Republic, m.sedlar@sigma.cz, t.kratky@sigma.cz
[2]Institute of Thermomechanics of the CAS, v. v. i.
Dolejškova 5, Praha 8, 182 00, Czech Republic, zimap@it.cas.cz

Abstract

This work presents the numerical investigation of an unsteady cavitating flow around a balancing drum of a multistage pump. The main attention is focused on the cavitation phenomena, which occur in the rear part of the drum clearance, cause the erosion of the drum material and influence the pressure losses and the flow rate through the clearance. The one-way coupling of the URANS equations and the full Rayleigh-Plesset equation is employed to analyse the flow field as well as the dynamics of cavitating bubbles. The numerical simulations show that the erosion processes are highly influenced by shaft vibrations, namely by periodic deformations of the annular clearance in time. The calculated results are verified by erosion tests on a real pump.

Keywords: cavitation erosion, numerical simulation, multistage pump, balancing drum

1. Introduction

The assessment of cavitation erosion inside hydrodynamic machinery still represents a challenge for the users and developers of CFD tools. While the degradation of machine performance due to cavitation or cavitation surge can be analysed satisfactorily in many cases using standard CFD tools [1-8], modelling the cavitation erosion is, however, somewhat more difficult. The erosive potential of the cavitating flow is carried by the violent collapses of vapour bubbles in the vicinity of the solid surface and is a consequence of either the effect of the shock waves propagated from the centre of the collapsing bubble or the liquid micro-jet formed during the non-spherical bubble collapse, or the combination of both [9]. The time scale of the bubble collapse is several orders of magnitude lower than the time scale used in the URANS (Unsteady Reynolds-Averaged Navier-Stokes) equations for the flow field analysis. In addition, to capture the bubble collapses and rebounds a complex form of the Rayleigh-Plesset (R-P) equation must be employed. The standard CFD tools based on the Euler-Euler approach can integrate only a very simplified R-P equation, in which the higher-order terms are neglected. Such a simplification does not allow us to predict the rebounds of the cavitation bubbles or the position and energy of the bubble collapses. The cavitating flow behaviour is also very sensitive to the nuclei content. Nevertheless, in CFD applications the dependence of cavitation on the nuclei content is typically neglected or highly simplified (usually only one size of the initial nuclei radius is considered).

In our approach we use the Euler-Lagrange approach to couple the CFD analysis of the turbulent flow with the analysis of the spherical bubble dynamics using the full R-P equation along carefully selected trajectories. It is assumed that the liquid (water) flowing through the hydraulic parts contains a known number of air-filled or vapour-filled microbubbles of the known size distribution. The authors used this approach previously for a steady-state flow as described in [10-12]. The influence of the bubble breakup during the collapse was later taken into account in [13-14]. The effects of flow unsteadiness and bubble-bubble interaction were added to the model and described in [15]. For the unsteady analysis the steady-state streamlines are replaced by bubble trajectories. The bubble-bubble interaction is taken into account by superposing the pressure change due to the pressure waves generated by the collapsing bubbles at different positions in the flow and propagated in the computational domain over the local pressure in the liquid (external to the bubble). The numerical model described in [10-15] is based on the two-way coupling. Both the CFD analysis and the analysis of the spherical bubble dynamics are performed using the in-house software.

Because the two-way coupling of the URANS and R-P equations for complex geometries is computationally highly expensive, we offer a simplified approach in this work. The approach is based on the one-way Euler-Lagrange coupling, in which the highly efficient ANSYS CFX tool is used in the first stage of the analysis.

Received October 19 2015; accepted for publication November 23 2015: Review conducted by Tadashi Tanuma, PhD. (Paper number O15055S)
Corresponding author: Milan Sedlář, Dr., m.sedlar@sigma.cz

This paper was presented at 13th Asian International Conference on Fluid Machinery (AICFM), September 7-10, 2015, Tokyo, Japan

2. Cavitation Erosion Model

As mentioned earlier the erosive effect of the cavitation flow is modelled using the one-way coupling of the CFD analysis of the 3D unsteady turbulent flow with the analysis of the cavitation bubble dynamics along selected trajectories. In the bubble dynamics model we use the R-P equation in the following form:

$$R\frac{D^2R}{Dt^2}+\frac{3}{2}\left(\frac{DR}{Dt}\right)^2+\frac{4\nu_e}{R}\frac{DR}{Dt}+\frac{2\sigma}{\rho_L R}\left[1-\left(\frac{R_0}{R}\right)^{3\kappa-1}\right]=\frac{p_v-p_0}{\rho_l}\left[1-\left(\frac{R_0}{R}\right)^{3\kappa}\right]+\frac{p_0-p}{\rho_l}+\frac{R}{\rho_l c_l}\frac{D}{Dt}(p_g-p)\,. \tag{1}$$

Here, p_0 is the liquid ambient pressure at undisturbed initial condition, p_v is the equilibrium vapour pressure, p_g is the pressure of the gas mixture inside the bubble, ρ_l is the liquid density, c_l is the sound velocity of the liquid, σ is the surface tension of the liquid and κ is the polytropic index for the gas mixture inside the bubble. ν_e represents the "effective" viscosity, which is taken as an empirical multiple of the kinematic viscosity. In the following calculations the gas inside the bubbles is assumed to behave isothermally, i.e. $\kappa = 1$. In order to model bubble rebounds the bubble must contain some gas [9]. Therefore, it is assumed that the bubble interior is formed by a mixture of non-condensable gases obeying the following laws:

$$p_g R^{3\kappa} = p_{g0} R_0^{3\kappa} \quad , \qquad p_{g0} = p_0 - p_v + 2\sigma/R_0\,. \tag{2}$$

Equation (1) is solved by the fourth-order Runge-Kutta scheme with the adaptive step-size algorithm.

The modelling of the erosion risk is based on the assumption that the main contribution to the erosion of solid materials arises from the mechanical effects of the collapsing bubble near the solid surface. These effects are represented by the impact of a spherical shock wave propagated from the centre of the collapsing bubble. The erosion potential of the shock wave is estimated from the energy dissipated during the collapse. For simplicity we neglect the energy emitted as the acoustic energy or used to evaporate/condense the vapour and heat up the non-condensable gas inside the bubble. Let us denote the energy dissipated during the i-th collapse as ΔE_i. Let us also denote the work done by the pressure inside the bubble p_b against the ambient liquid pressure p to expand the bubble from the minimum radius $R_{min,i}$ to the maximum radius $R_{max,i}$ as $W_{growth.}$ We can estimate ΔE_i by subtracting W_{growth} for the $(i+1)$-th bubble expansion from W_{growth} for the i-th bubble expansion. The following holds if the effects of liquid viscosity, compressibility and surface tension are neglected:

$$\Delta E_i = W_{growth}\Big|_{R\min,i}^{R\max,i} - W_{growth}\Big|_{R\min,i+1}^{R\max,i+1}\,, \text{ where } W_{growth}\Big|_{R\min}^{R\max} = \int_{R_{min}}^{R_{max}} 4\pi R^2 (p-p_b)dR\,. \tag{3}$$

We further assume that only a part of the energy ΔE_i presents the erosive potential of the collapse disruptive to the solid wall. The erosive part of ΔE_i is denoted as E and can be expressed as $E = C\Delta E_i$, where C is a geometric parameter, which depends mainly on the distance of the bubble centre from the solid surface. For bubbles very far from the solid surface C tends to zero. In this analysis, $C = 0.25$ if the distance of the bubble centre from the solid surface is lower than the maximum radius of the bubble. When the distance is higher, the value of C decreases with the second power of the distance. The numerical algorithm is described in detail in the previous works [10-13].

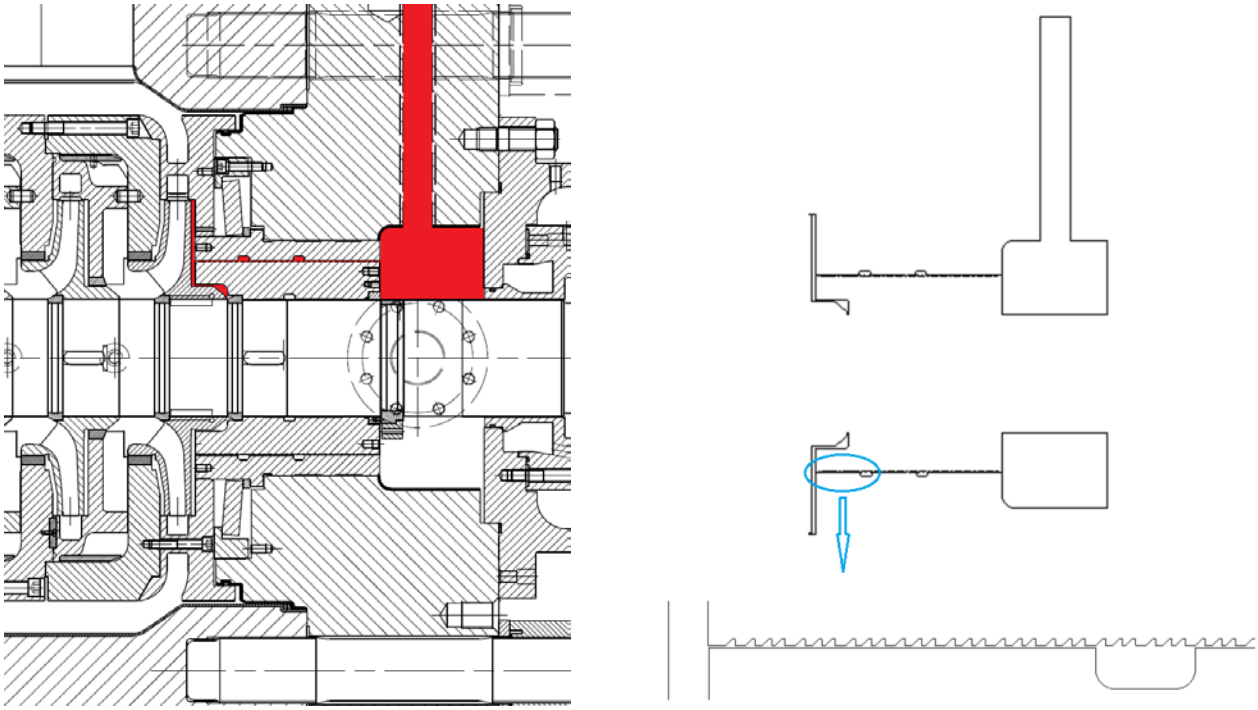

Fig. 1 Cross-section of balancing drum and computational domain

3. Cavitating Flow around Balancing Drum: Problem Definition

The computational domain consists of the clearance and the attached chambers of the balancing drum, which is placed behind the last impeller of the multistage pump (Fig. 1). The rotating wall of the drum is equipped with a system of 97 grooves. There are two large chambers in the stator part of the clearance. The liquid (water) passing through the clearance is conducted away to the pump suction by a circular channel (Fig. 2) and a piping (which is not included in the numerical simulation itself).

The computational grid is multi-block structured, with approximately 3 mil. nodes. At the inlet to the computational domain (located behind the last impeller, Figs. 1, 3) the total pressure is set. At the outlet (end of the circular channel) the flow through the balancing drum clearance is prescribed. The flow is adjusted during several iterations so that the average static pressure at the outlet (plus estimated pressure losses in the whole piping system behind the drum) reaches the value prescribed at the pump suction.

In the first step, the ANSYS CFX package is used to solve the URANS equations coupled with the simplified Rayleigh-Plesset cavitation model included in the ANSYS CFX package. This simplified model is used to describe the interphase mass transfer within the homogenous multiphase model. The turbulence is modelled using the SST model. In the second step, the methodology described in Chapter 2 is employed to monitor the dynamics of the cavitating bubbles as well as their collapses and the cavitation erosion potential. The number and size of the initial cavitation nuclei are determined empirically (see the next section). The bubble-bubble interactions are not considered.

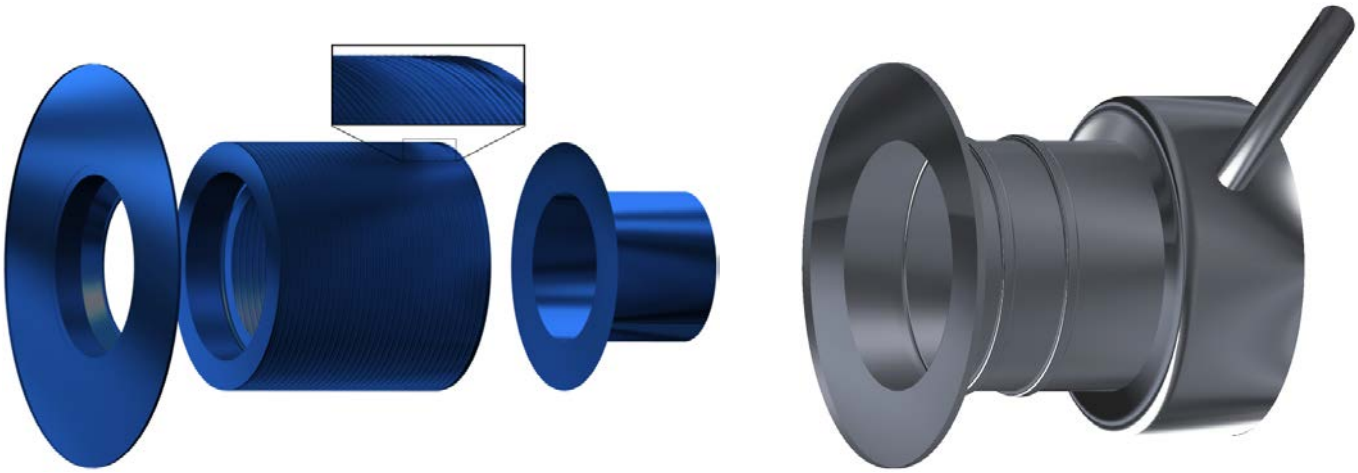

Fig. 2 Rotating part of balancing drum (left, in dark blue) and stator part (right, in grey)

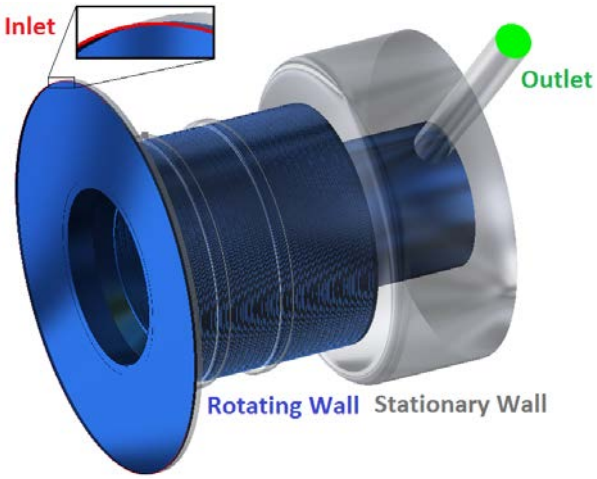

Fig. 3 Description of boundary conditions

Fig. 4 Grooved drum surface with signs of cavitation erosion in the rear part

4. Results and Discussion

The main motivation for this study is to explain the appearance of cavitation damage (pits) on the grooved surface of the drum, in the last 40 mm of the clearance (Fig. 4) during the pump tests. A comprehensive CFD analysis has been performed for the existing standard design (Variant 1) of the clearance. This variant has a constant clearance of 0.35 mm (measured between the stator wall and the tooth tip).

The numerical simulations show that the flow rate through the clearance is highly influenced by the cavitation phenomena. For the optimal pump flow rate Q_{pump_opt} as well as the suboptimal ones a cavitation region is formed in the very end of the clearance. The cavitation region acts as a plug filling the whole outlet of the clearance and disappears in the chamber downstream of the

clearance (top of Fig. 5). The cavitation region increases the clearance resistance and decreases the flow rate. To avoid the danger of cavitation erosion in the clearance, a second variant has been designed. The new design (Variant 2) features an increased gap height of 0.5 mm in the last 50 mm of the clearance, on the side of the stator wall (Fig. 6). The diffused gap significantly reduces the cavitation region in the clearance outlet. As a result the cavitation region no longer fully fills the clearance outlet for any pump flow rate (bottom of Figure 5). On the other hand the flow rates through the clearance are increased (Fig. 7). Figure 8 compares the pressure distribution on the rotor part of the clearance for non-cavitating and cavitating flows through the standard clearance and demonstrates the influence of the increased gap in the rear part of the clearance for 50% of the optimal pump flow rate.

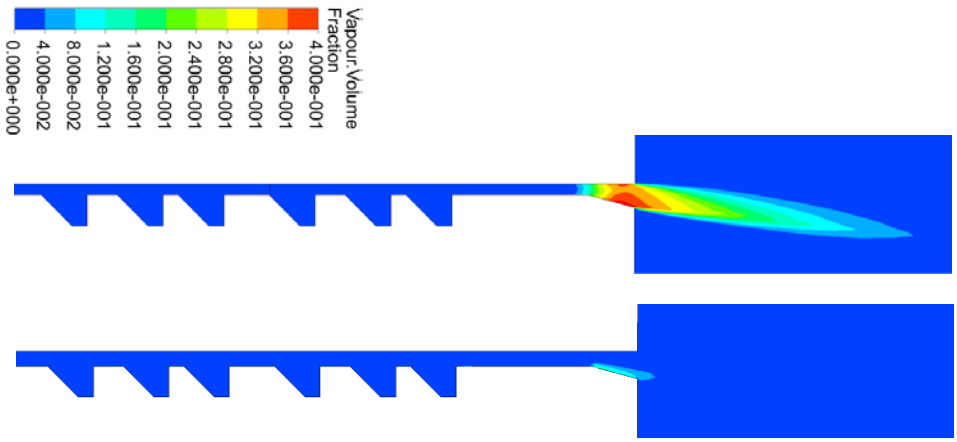

Fig. 5 Cavitation regions in the rear part of clearance. Variants 1 (top) and 2 (bottom) as defined in Fig. 6. Q = 0.5 Q_{pump_opt}. Shaft vibrations neglected

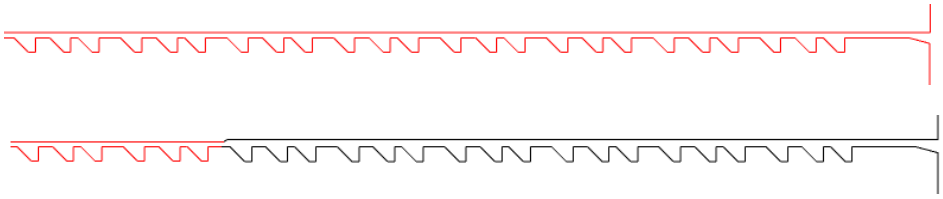

Fig. 6 Standard clearance (Variant 1, top) and clearance with increased gap in the rear part (Variant 2, bottom). Detail of the rear part. Change of geometry is indicated in black

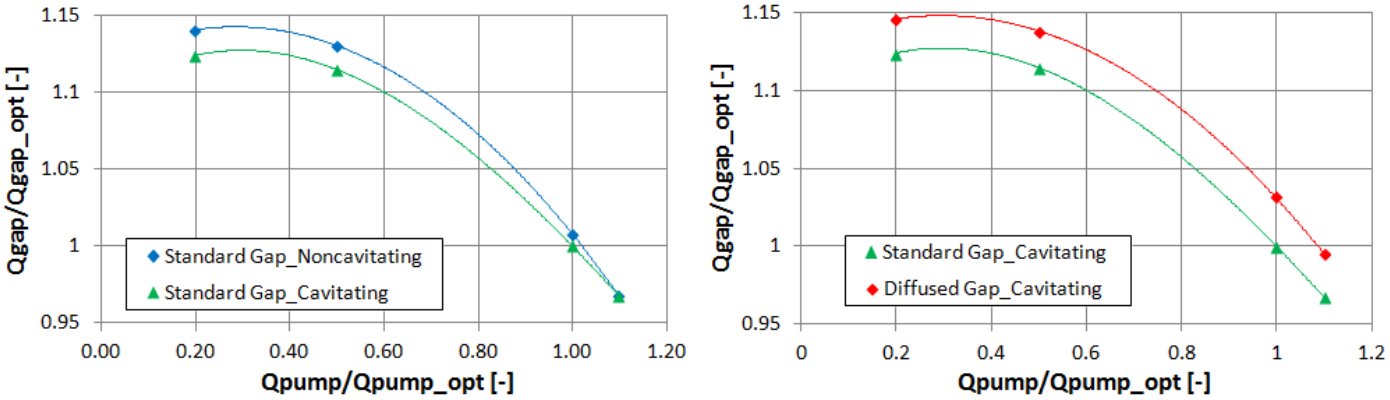

Fig. 7 Normalised flow rate through clearance based on normalised pump flow rate. Non-cavitating and cavitating flow through standard clearance (left) and influence of increased/diffused gap in the rear part of clearance (right). Shaft vibrations neglected

The CFD analysis presented above cannot explain the cavitation erosion observed in Fig. 4. The reasons are the following: the flow is considered quasi-steady; the geometry of the clearance does not change and remains perfectly annular. In reality, the shaft is bending between the bearings and the annular gap deforms periodically in time. In order to take into account the change of geometry due to the shaft deformation we have implemented a simple model of the shaft vibrations, in which the entire grooved surface of the drum oscillates periodically in the same direction and amplitude. The oscillation is harmonic with the maximum amplitude equal to three quarters of the clearance height. The oscillations cause changes of the static pressure, which then give rise to the appearance of cavitation bubbles in the rear part of the clearance. Figure 9 shows the void fraction distribution in two cross-sections of the clearance at the same time step for the suboptimal flow rate of the pump Q = 0.5 Q_{pump_opt}. The first cross-section has been selected to demonstrate the most intensive cavitation in the very end of the clearance, whereas the second cross-

section has been selected to demonstrate the least intensive cavitation. Graphs in Fig. 10 show the corresponding pressure distributions on the rotor part of the clearance.

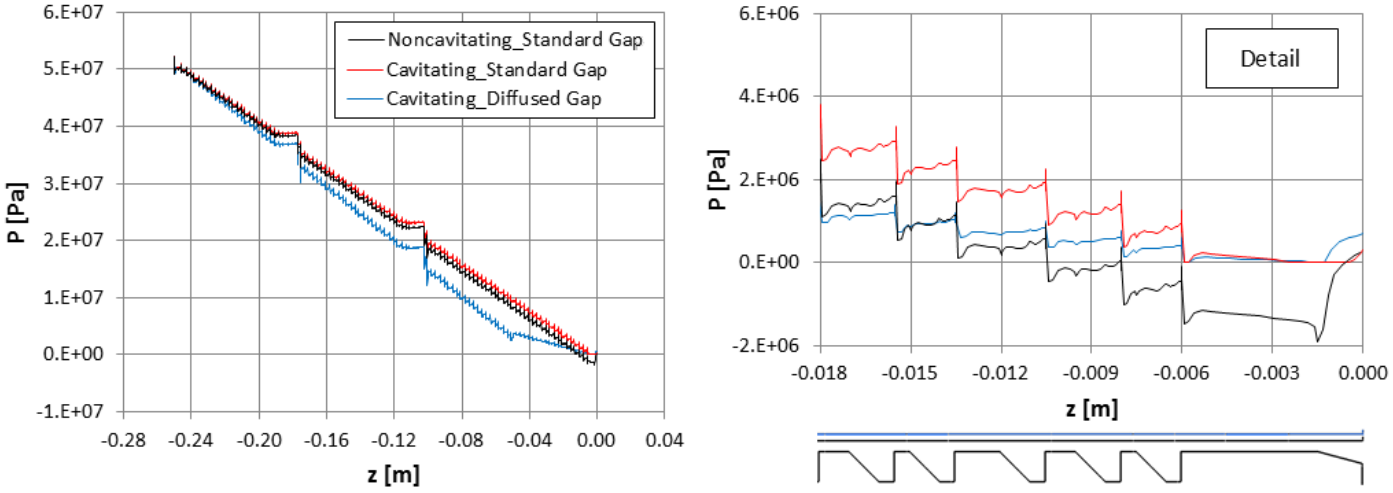

Fig. 8 Pressure distribution in the rotor part of clearance. Non-cavitating and cavitating flow through standard clearance and influence of increased gap in the rear part of clearance; z is the distance along axis of revolution. Q = 0.5 Q_{pump_opt}. Shaft vibrations neglected

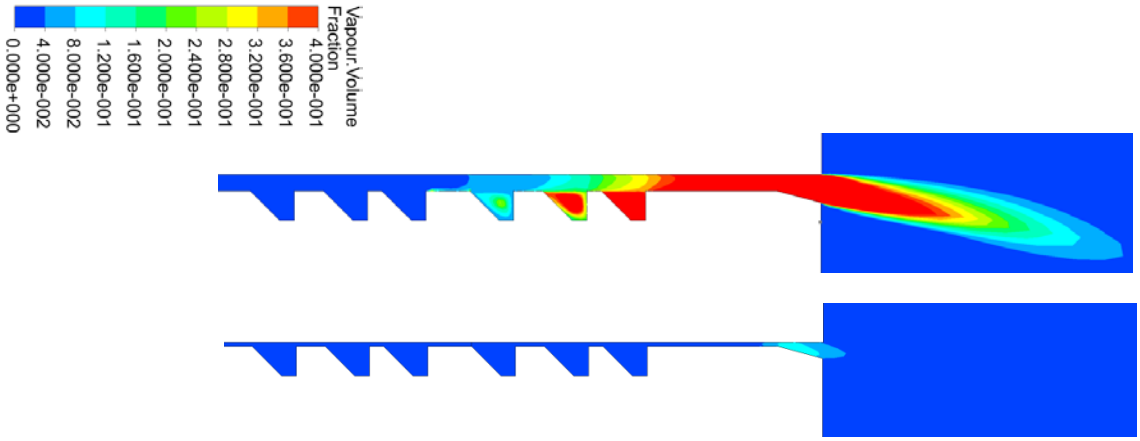

Fig. 9 Cavitation regions in the rear part of clearance at the same time step. Upper cross-section has been selected to demonstrate the most intensive cavitation, the lower to demonstrate the least intensive cavitation. Q = 0.5 Q_{pump_opt}. Variant 1, shaft with maximum deflection due to vibrations

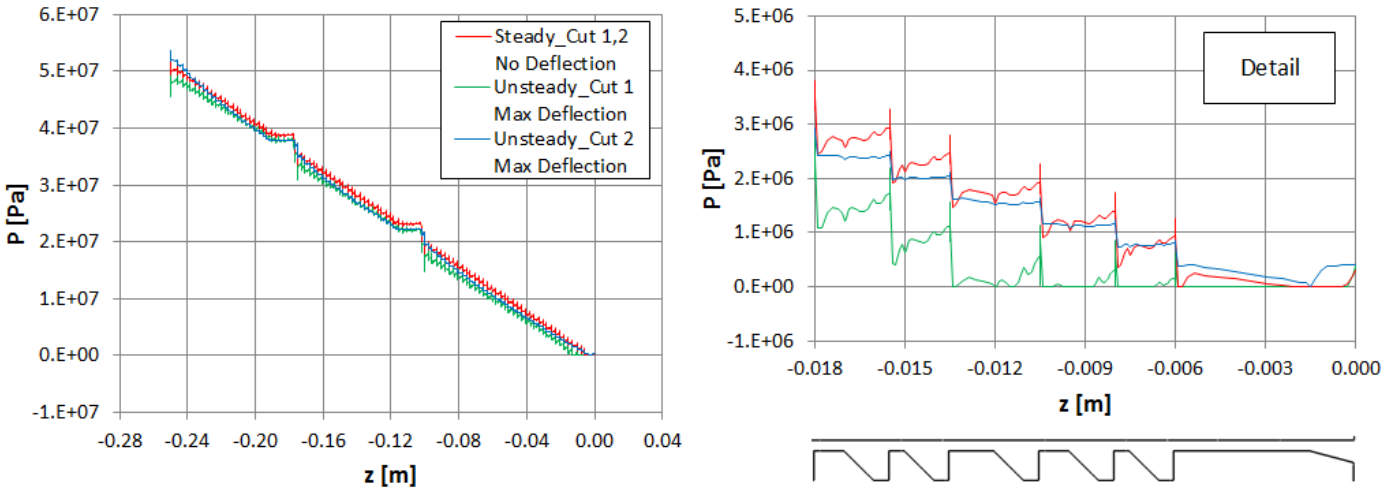

Fig. 10 Pressure distribution on rotor part of clearance corresponding to Fig. 9

The results of the CFD analysis are used to provide the input data for the subsequent cavitation risk analysis. A system of trajectories has been generated to monitor the dynamics of the cavitating bubbles including their collapses. Two types of

trajectories can be observed close to the drum surface (Fig. 11). The first type (violet line) represents the trajectories passing smoothly through the clearance along the drum. The second type (orange line) represents a surprisingly stable flow in the drum grooves. Clearly, there are also trajectories which switch from one type to the other, however, because we are interested in the relatively short section at the end of the clearance the first type must be treated with the methodology described in Chapter 2. Figure 12 compares the pressure distribution along such a trajectory passing through the region with the lowest pressure with the pressure on the drum surface corresponding to the sections shown in Figs. 9 – 10.

The bubble dynamics has been calculated for ten initial bubble sizes. The empirical bubble size distribution (Fig.13) is based on the measurements performed in the test rig of the Centre of Hydraulic Research using the acoustic bubble spectrometer [12] and on the tests and experience of other authors [9], [16]. The cavitation nuclei are sized in the range from 2.5 μm to 45 μm. There are two reasons for this range of sizes. First, it has been shown [12-13] that the largest contribution to the erosive potential comes from the cumulative effect of the bubbles with the initial size of about 15 μm and this finding will be demonstrated in the following figures. The second reason is that the bubbles with the initial size larger than 35 μm grow to a size comparable with the clearance height. Such bubbles cannot resist the shear stress between the mutually moving walls of the clearance and consequently break up. This mechanism is not captured well in this study. On the other hand, the break-up of the bubbles during their collapse is modelled using the Rayleigh-Taylor instability analysis [13-14]. Figure 14 shows the dynamics of bubbles for five initial bubble sizes along the trajectory of the first type (violet line from Fig. 11), passing through the region with maximum cavitation. The dynamics is rather complicated as the bubbles pass through several pressure peaks (Fig. 12). One can notice several bubble break-ups during the first collapses and also during the subsequent collapses (especially for bubbles with the initial sizes 20 μm and 40 μm, z = 0.002 m and z = 0.0043 m). The bubbles of the initial size of 40 μm are found to break up at the position z = –0.0013 m where they fission into nine fragments each due to the shear stress between the moving walls. As we consider the total volume of all the fragments equal to the volume of the parental bubble, the radius of fragments is 2.08 ($9^{1/3}$) times lower. Figure 15 shows the corresponding cumulative erosion potential of all bubbles of the same size associated with the bubble collapses. The most important erosion potential can be assigned to the bubbles with the initial size of about 15 μm (due to the synergy between their relatively significant count in the nuclei size distribution and the strength of their collapse). Generally, the highest erosion potential (more than 10 W/m^2) comes from the collapses downstream of the clearance and can be disregarded as being outside of our region of interest, however, there is still a notable erosion potential of about 1 W/m^2 close to and behind the last three grooves.

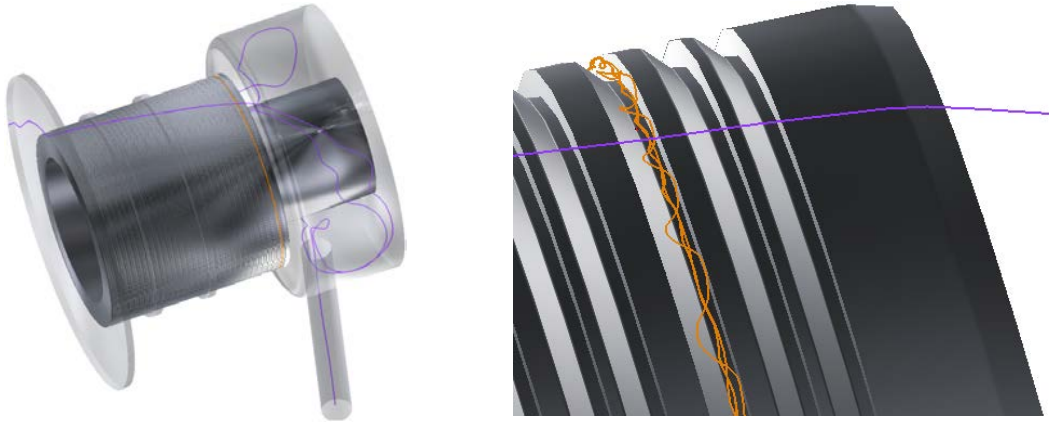

Fig. 11 Two typical types of trajectories close to drum surface. Variant 1, Q = 0.5 Q_{pump_opt}

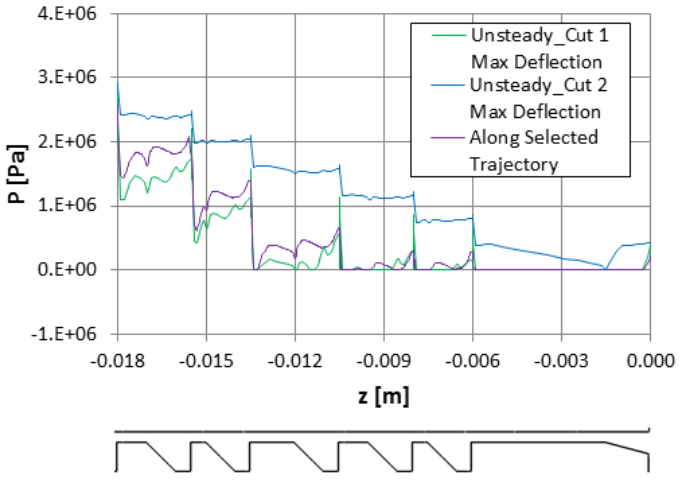

Fig. 12 Detail of pressure distribution along selected trajectory compared to pressure on drum surface corresponding to Figs. 9 – 10

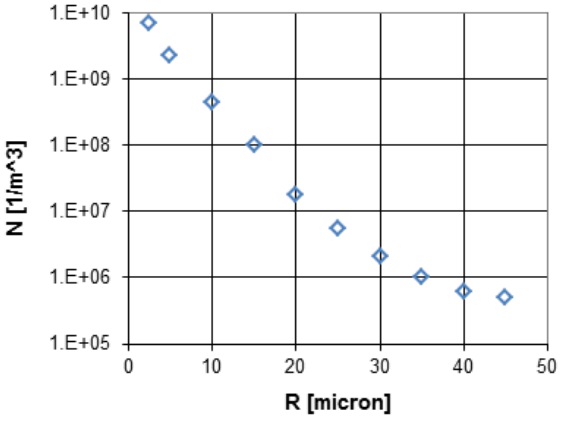

Fig. 13 Nuclei number density distribution used in presented analysis

As mentioned earlier the most important are the bubbles along the first type of trajectories, which pass smoothly through the clearance along the drum (Fig. 11). Moreover, any protrusion or damage on the sharp edges of the grooves can initiate local cavitation. Therefore, one can expect that the eroded pattern should take a form of stripes, which are not parallel with the axis of revolution but instead have the direction of the trajectories. Figure 16 compares the estimated pattern of the cavitation erosion on the drum surface based on the presented numerical simulation (left) with the cavitation erosion observed during the tests on the real pump. The picture on the left hand side has been obtained very simply: it depicts trajectories passing through points randomly distributed on the drum surface endangered by cavitation erosion.

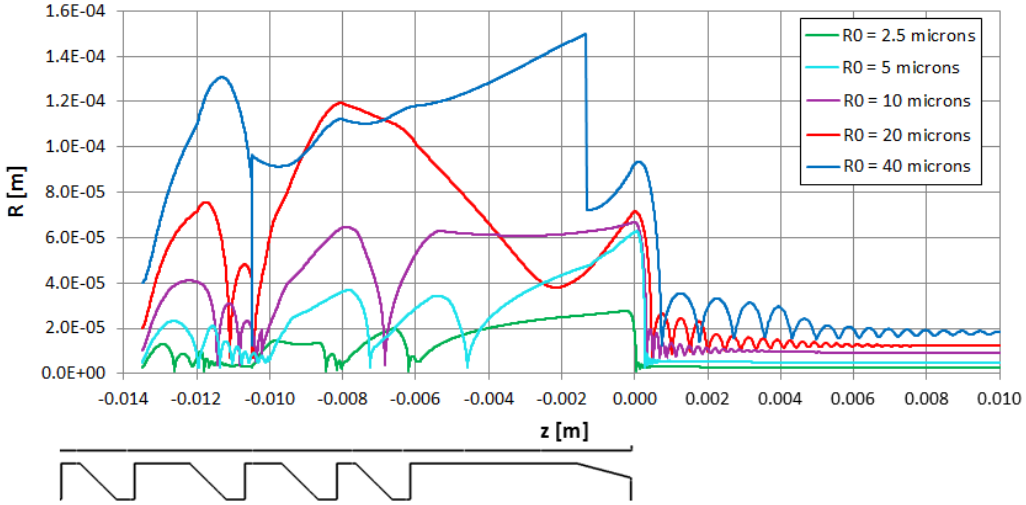

Fig. 14 Dynamics of bubbles with different initial sizes along the violet trajectory from Fig. 11

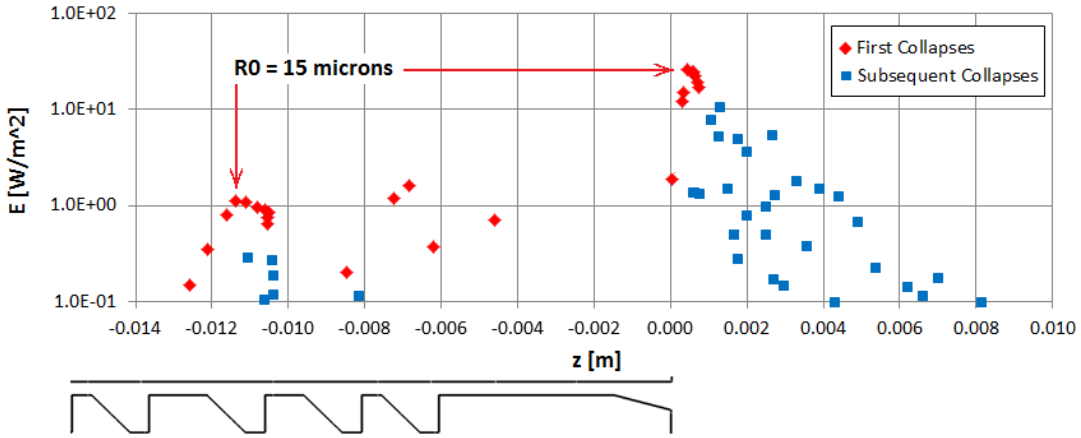

Fig. 15 Erosion potential of all bubbles along the violet trajectory from Fig. 11

Figure 5 has demonstrated that the diffused gap with the gap height of 0.5 mm in the last 50 mm of the clearance (Variant 2) significantly reduces the cavitation region in the clearance outlet. We will now perform the analysis of the bubble dynamics for the changed geometry for conditions similar to Variant 1. Figure 17 compares the pressure distribution along the trajectories featuring the most intensive cavitation for standard and diffused gaps and the flow rate Q = 0.5 Q_{pump_opt}. The dynamics of bubbles for five initial bubble sizes along the trajectory in the case of Variant 2 can be seen in Fig. 18. It should be noticed that the results are (similar to Fig. 14) shown only for $z \geq -0.0135$ m, where we can expect strong bubble collapses due to the pressure drop below the equilibrium vapour pressure p_v. For $z < -0.0135$ m the bubbles oscillate with their natural frequency due to the complicated pressure distribution on the drum surface. Typically, we start our bubble-dynamics analysis several grooves before the first drop of the static pressure below p_v, as the integration of Eqs. (1) – (3) along the large set of full-length trajectories is computationally expensive. Figure 19 shows the corresponding cumulative erosion potential of all bubbles of the same size associated with the bubble collapses along the selected trajectory. The most important erosion potential can be assigned to the bubbles with the initial size of about 15 - 20 µm. When compared to Fig. 15 we can see that the highest erosion potential has decreased by about one order of magnitude.

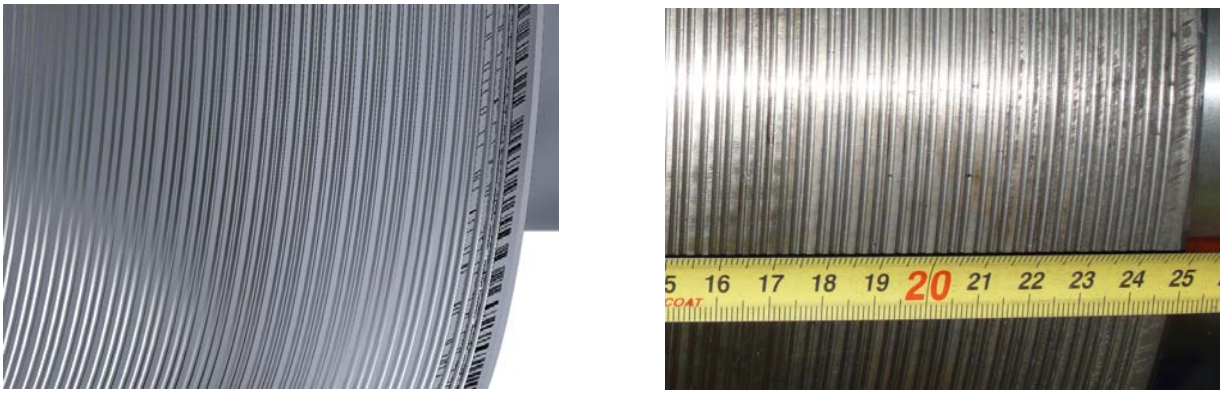

Fig. 16 Grooved drum surface with signs of cavitation erosion in the rear part.
Numerical simulation (left) and tests (right)

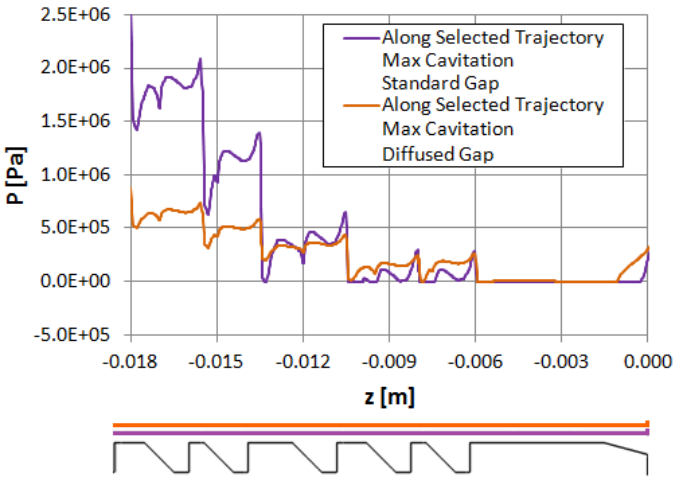

Fig. 17 Detail of pressure distribution along selected trajectories featuring the most intensive cavitation for standard and diffused gaps. Q = 0.5 Q_{pump_opt}.

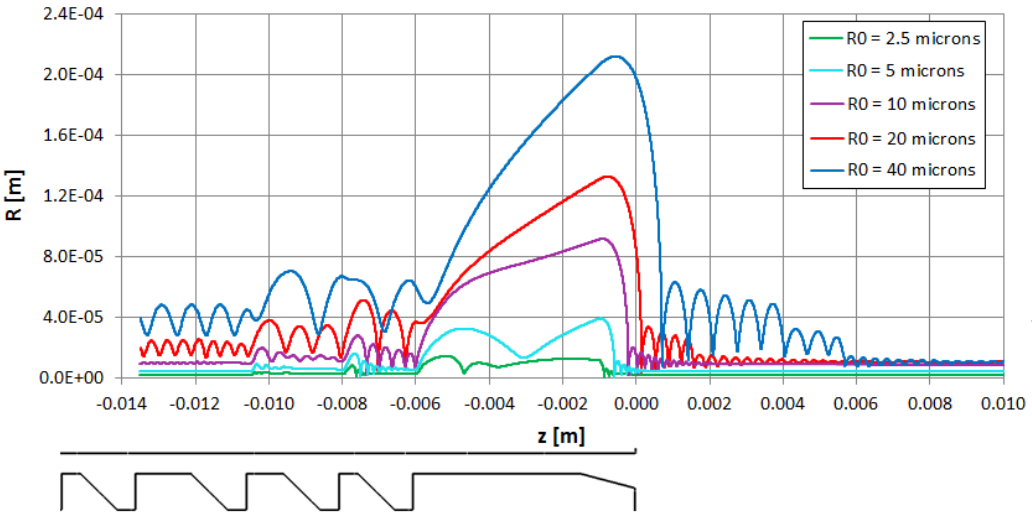

Fig. 18 Dynamics of bubbles with different initial sizes along the trajectory featuring the most intensive cavitation.
Diffused gap. Q = 0.5 $Q_{pump\_opt.}$

5. Conclusion

The numerical model presented in this paper predicts the erosion potential of a three-dimensional unsteady turbulent cavitating flow using a computationally efficient method combining the commercially available ANSYS CFX package for the 3D flow analysis and the Lagrange-based in-house software for the analysis of the erosive potential of cavitation bubbles.

This work is focused on the cavitation phenomena occurring in the rear part of the balancing drum of a multistage pump and causing the erosion of the drum material. The cavitation phenomena also play an important role in the pressure losses and

influence the flow rate through the clearance. The rotating wall of the drum is equipped with a system of grooves with sharp edges. Two variants of the clearance geometry have been analysed. The standard design (Variant 1) has a constant gap height of 0.35 mm and shows significant cavitation erosion in its rear part. It has been found that the shaft vibrations enhance cavitation and therefore careful attention should be paid to optimising the system of bearings to prevent shaft vibrations especially in the rear part of the balancing drum. The improved design (Variant 2) with the increased gap height of 0.5 mm in the last 50 mm of the clearance features a remarkably reduced cavitation region in the clearance outlet and reduced cavitation erosion potential even for regimes, where the grooved surface of the drum oscillates periodically. A schematic evaluation of the cavitation erosion risk for both variants can be seen in Fig. 20. It is based on the evaluation of the erosion potential of all bubbles along all selected trajectories.

The calculated results have been verified qualitatively by erosion tests on a real pump with the balancing drum for Variant 1. The cavitation damage (i.e. the pattern of pits) appears in the last 40 mm of the clearance, while the numerical analysis estimates the damage only in the last 13 mm. The difference can be caused by several reasons. First, any protrusion or damage on the sharp edges of the grooves can initiate local cavitation even in the regions where the numerical simulation (with the perfect geometry) gives the static pressure larger than the equilibrium vapour pressure. Second, we must take into account the very simplified model of the shaft oscillations. Third, the damage pattern can develop with time, which is a concept that is not considered in the presented erosion risk analysis. And last but not least, we have used the URANS equations with the turbulence model, which is known to be unable to predict complicated pattern of turbulent eddies along the groves, which could initiate local cavitation. For this purpose, the Large Eddy Simulations (LES) could be used, however they are computationally highly expensive and still far from the current engineering practice.

The values of the erosion potential *E* are quantitative, however they must be calibrated against the experimental data. Currently, the model is unable to link erosion risk with the erosion rate (mass loss rate due to cavitation erosion) of different materials.

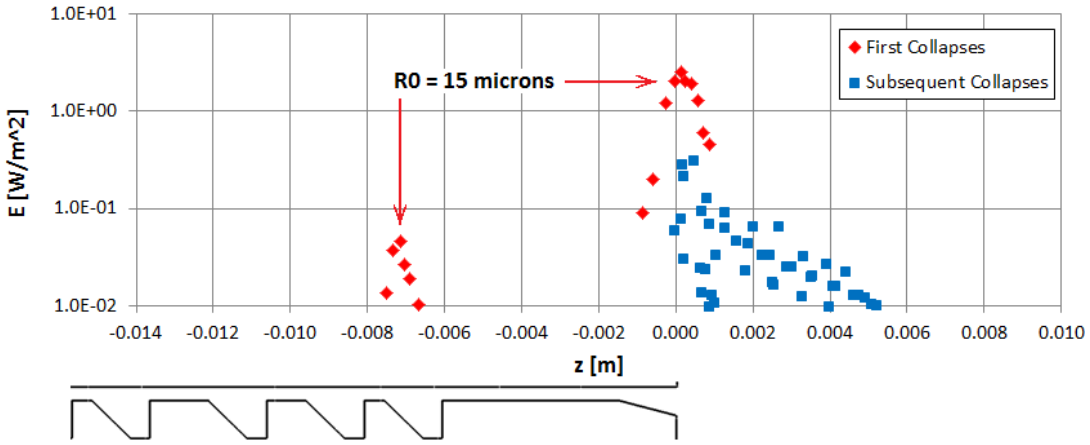

Fig. 19 Erosion potential of all bubbles along the trajectory from Fig. 18

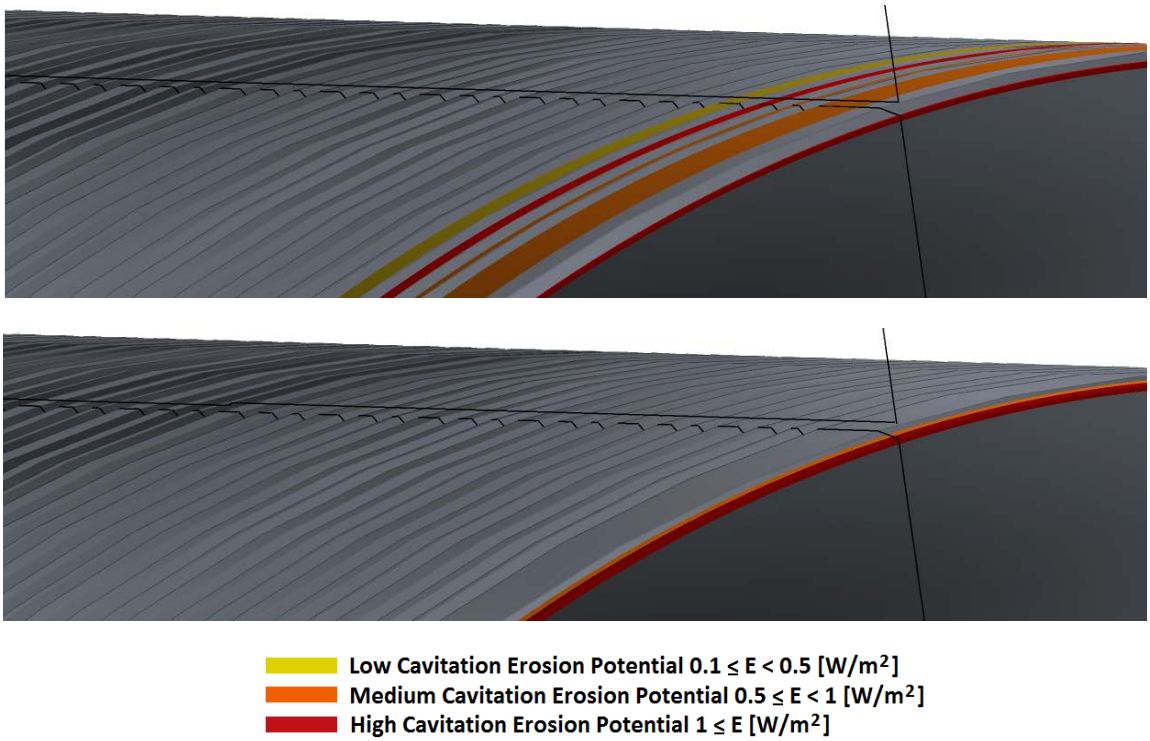

Fig. 20 Schematic evaluation of cavitation erosion risk. Variant 1 (top) and Variant 2 (bottom)

Acknowledgments

This work has been supported by grant no. 101/13/23550S of the Czech Science Foundation, entitled “Experimental Research and Mathematical Modelling of Unsteady Phenomena Induced by Hydrodynamic Cavitation”. The authors would like to acknowledge also the institutional support RVO:61388998 of the Institute of Thermomechanics of the CAS, v. v. i.

Nomenclature

E	Cavitation erosion potential [W/m^2]	Q_{pump_opt}	Optimal pump flow rate [m^3/s]
c_l	Sound velocity of liquid [m/s]	R	Bubble radius [m]
p	Static pressure [Pa]	R_0	Initial bubble radius [m]
p_0	Liquid ambient pressure [Pa]	z	Distance along axis of rotation [m]
p_g	Pressure of gas mixture inside bubble [Pa]	W_{growth}	Work done by the pressure inside the bubble
p_v	Vapour pressure [Pa]		
Q_{gap}	Flow rate through drum clearance [m^3/s]	κ	Polytropic index for gas mixture [-]
Q_{gap_opt}	Flow rate through drum clearance	ν_e	Effective viscosity [m^2/s]
	at pump optimal flow rate [m^3/s]	ρ_l	Liquid density [kg/m^3]
Q_{pump}	Pump flow rate [m^3/s]	σ	Surface tension [N/m]

References

[1] Berntsen, G., Kjeldsen, M., and Muller, R., 2001, “Cavitation Induced Dynamics in Hydraulic Machinery,” Proc. 10th IAHR WG Meeting on the Behaviour of Hydraulic Machinery under Steady Oscillatory Conditions, pp. 1-8.
[2] Bouziad, Y. A., 2005, “Physical Modelling of Leading Edge Cavitation: Computational Methodologies and Application to Hydraulic Machinery,” Thesis No. 3353, Ecole Polytechnique Federale de Lausane.
[3] Tsujimoto, Y., 2005, “Tip Leakage and Backflow Vortex Cavitation,” Proc. CISM Advanced School on Fluid Dynamics of Cavitation and Cavitating Turbopumps.
[4] Yamamoto, K., and Tsujimoto, Y., 2009, “Backflow Vortex Cavitation and Its Effects on Cavitation Instabilities,” Int. Journal of Fluid Machinery and Systems, Vol. 2, No. 1, pp. 40-54.
[5] Oh, H.W., 2010, “Design Parameter to Improve the Suction Performance of Mixed-Flow Pump Impeller,” Proc. IMechE, Part A: Journal of Power and Energy, Vol. 224, No. 6, pp. 881-887.
[6] Kobayashi, K., and Chiba, Y., 2010, “Computational Fluid Dynamics of Cavitating Flow in Mixed Flow Pump with Closed Type Impeller,” Int. Journal of Fluid Machinery and Systems, Vol. 3, No. 2, pp. 113-121.
[7] Tsujimoto, Y., Horiguchi, H., and Yonezawa, K., 2010, “Cavitation Instabilities in Turbopump Inducers. Analyses in 1-3 Dimensions,” Int. Journal of Fluid Machinery and Systems, Vol. 3, No. 2, pp. 170-180.
[8] Sedlář, M., Šputa, O., and Komárek, M., 2012, “CFD Analysis of Cavitation Phenomena in Mixed-Flow Pump,” Int. Journal of Fluid Machinery and Systems, Vol. 5, No. 1, pp. 18-29.
[9] Franc, J. P., and Michel, J. M., 2004, Fundamentals of Cavitation, Kluwer Academic Publishers, Dordrecht.
[10] Sedlář, M., Maršík, F., and Šafařík, P., 2000, “Modelling of Cavitated Flows in Hydraulic Machinery Using Viscous Flow Computation and Bubble Dynamics Model,” Proc. Fluid Dynamics 2000, pp. 107-110.
[11] Zima, P., Sedlář, M., and Maršík, F., 2005, Water, Steam, and Aqueous Solutions for Electric Power, Advances in Science and Technology: “Bubble Creation in Water with Dissolved Gas: Prediction of Regions Endangered by Cavitation Erosion,” Maruzen Co. Ltd., Kyoto, pp. 232-235.
[12] Zima, P., Sedlář, M., and Muller, M., 2009, “Modeling Collapse Aggressiveness of Cavitation Bubbles in Hydromachinery,” Proc. 7th Int. Symposium on Cavitation, CAV 2009, pp. 1-7.
[13] Zima, P., and Sedlář, M., 2012, “Modeling Bubble Collapse Aggressiveness in Travelling Bubble Cavitation Using Bubble Breakup Model,” Proc. 8th Int. Symposium on Cavitation, CAV 2012, pp. 182-186.
[14] Delale, C. F., Pasinlioglu, S., and Zima, P., 2012, “A Criterion for the Occurrence of Bubble Fission and Its Modeling,” Proc. 8th Int. Symposium on Cavitation, CAV 2012, pp. 78-82.
[15] Sedlář, M., Zima, P., and Komárek, M., 2014, “Numerical Prediction of Erosive Potential of Unsteady Cavitating Flow around Hydrofoil,” Appl. Mechanics and Materials, Vol. 565, pp. 156–163.
[16] Waniewski, T. A., Hunter, Ch., and Brennen, Ch., 2001, “Bubble Measurement Downstream of Hydraulic Jumps,” Int. Journal of Multiphase Flow, Vol. 27, Issue 7, pp. 1271-1284.